Applied Physics A (2022) 128:294
https://doi.org/10.1007/s00339-022-05414-2

Applied Physics A
Materials Science & Processing

Molecular dynamics study on the nanoscale repeated friction and wear mechanisms of TiC/Ni composites

Min Zheng[1] · Dingfeng Qu[1] · Xingchun Wei[1] · Zhou Zhang[1] · Zongxiao Zhu[1] · Linjun Wang[1] · Weihua Chen[1]

Received: 7 December 2021 / Accepted: 1 February 2022 / Published online: 13 March 2022

Abstract
In this study, the molecular dynamics method was used to simulate the process of repeated friction of TiC/Ni composites under a hard diamond grinding ball and the mechanical properties of abrasion depth and morphology, wear rate, atomic displacement, internal defect evolution, and temperature, were systematically investigated during multiple friction processes. It was found that when the action of the grinding ball on the workpiece is transmitted to the TiC phase, extreme value of friction force appears, the depth of the abrasion marks is shallow, the number of atoms in the workpiece that undergo large displacements is low, the atoms exhibit a tendency to bypass the TiC phase for displacement, and the TiC is subjected to external action energy, which leads to an increase in temperature and discontinuity in the workpiece temperature distribution. During repeated friction processes, the friction force reaches a maximum, the friction coefficient fluctuates drastically, the increment in the abrasion depth decreases, the large structural defects generated by initial friction events are decomposed into small structural defects or stable laminar dislocation tetrahedral structures leading to the formation of dislocation entanglement which improves the overall wear resistance of the workpiece, the temperature of the TiC increases rapidly, and the temperature difference compared to the substrate gradually increases.

Keywords Molecular dynamics simulation · Nickel-based composites · Friction and wear · TiC

1 Introduction

Nickel matrix composites have good high-temperature strength, thermal fatigue resistance, oxidation resistance, and thermal corrosion resistance. They are novel types of composite materials that are used to manufacture important heat components in aerospace, ships, and industrial gas-turbine engines [1–4]. In particular, nickel matrix composites doped with carbide phases combine the excellent properties of ceramics and nickel matrix materials, and nickel matrix titanium carbide composites are mainly used in high-temperature components with high processing and mechanical property requirements [5]. Such composites are of great importance for the development of industrial materials because they retain the characteristics of low mass, high-temperature resistance, high hardness, and corrosion resistance of ceramic materials, without compromising the high performance of nickel-based materials [6–11]. However, nickel-based titanium carbide composites often fail under actual service conditions from mechanical wear [12] and the strengthening mechanisms of carbides on nickel-based metal materials are unknown. Therefore, an in-depth study of the frictional wear behavior of nickel-based composites is of great scientific importance.

Traditional friction experiments mainly simulate the friction and wear of materials based on actual working conditions, and infer friction and wear mechanisms from the analysis of friction products, friction surface morphologies, and the influence of wear on structural characteristics [13, 14]. In response to the limitations of traditional means of friction test analysis, molecular dynamics simulation bridges the gap between the macroscopic and microscopic nature of materials with the advantages of high operational efficiency and simulation systems of large. It can compensate for the shortcomings of actual experiments by constructing more ideal models and quantifying the dynamic processes that occur in real solids online. At the same time, the surrounding environmental conditions and the properties of the material can be easily changed according to the needs of the research.

✉ Zongxiao Zhu
zhuzongxiaolut@163.com

[1] School of Mechanical and Electrical Engineering, Lanzhou University of Technology, Lanzhou 730050, China

In addition, the wear of materials is a continuous process in small increments with transient wear up to the micro/nanometer level. Therefore, it must be studied according to the basic units that make up materials. Molecular dynamics (MD) is promising for analyzing the motion of discrete atoms or molecules at the nanometer level. Additionally, the processes of dynamic migration and phase transitions of the material can be observed, including microscopic evolution [15–19] which can reveal the strengthening mechanisms and interfacial structures of reinforcement in nickel–matrix composites, as well as the frictional wear mechanisms of nickel matrix composites.

TiC carbide-reinforced nickel-based composites have been widely used in tools, molds, wear-resistant components, and high-temperature oxidation-resistant components [20]. Liu et al. [21] studied the effects of TiC nanoparticles on the microstructure and tensile properties of a Ni–Fe matrix. Various studies have demonstrated that as-cast grains are refined and yield strength, ultimate tensile strength, and elongation are improved by the presence of trace TiC nanoparticles. Testa et al. [22] obtained a composite coating through the mixed plasma spraying of a TiC suspension and dry Tribaloy-400. They found that the coating with 25 vol% TiC exhibited good performance in terms of hardness and toughness, and the sliding wear rate was approximately 10^{-6}–10^{-5} $mm^3/(N{\cdot}m)$. Lv et al. [23] mixed FeCrAl powder and TiC nanoparticles via directional energy deposition. Experimental results revealed that when the content of TiC particles was 3.5 wt.%, the yield strength of the alloy was 208 MPa, the tensile strength was 223 MPa, and the elongation was 53%, thereby, providing excellent mechanical properties. Wang et al. [24] prepared TiC-reinforced Inconel 718 composites using a selective laser melting technique. Experimental results demonstrated that the tensile strength and yield stress of the composites was improved. It was also observed that the TiC particles significantly refined the organization of Inconel 718 and that the reinforcing particles significantly hindered the growth of columnar crystals. Zhang et al. [25] added micro-amounts of in situ TiC nanoparticles to 40Cr steel. Experimental results revealed that the trace TiC nanoparticle/40Cr steels prepared using this method exhibited better room- and high-temperature properties than pristine 40Cr steel. Reddy et al. [26] prepared nanoscale SiC-reinforced aluminum matrix nanocomposites using microwave sintering and hot extrusion techniques. Experimental results demonstrated that the 5 vol% SiC nanocomposites exhibited the best mechanical and thermal properties. Cai et al. [27] prepared a graphite/CaF_2/TiC/Ni-base alloy composite coating using plasma spraying technology. Their research revealed that the friction coefficient of the composite coating was between 0.22 and 0.288, which is 25.9–53% lower than that of a pure nickel-based alloy coating. Its wear rate was also 18.6–70.1% lower than that of a pure nickel-based alloy coating. Yin et al. [28] studied the nano-wear behavior of SiC particle-reinforced aluminum matrix composites (SiC/Al-NCs) under the action of a spherical diamond indenter. They found that dislocation strengthening occurred in the nano-scratches on the SiC/Al-NCs. Zhang et al. [29] studied scratches on Al/Si composites using MD simulations. They found that the hardness and friction coefficient of the composites were equivalent to the average values of the two materials at the interface. Wang et al. [30] used MD to simulate the deformation behavior of single-crystal GaN processing. The effects of cutting speed, cutting depth, and abrasive particle shape on the atomic strain, stress, temperature, cutting force, and deformation layer were systematically studied. Hao et al. [31] used MD to simulate the diffusion mechanism of Ni-based superalloy Ni-Fe-Cr series nano-cutting tools and studied the interaction mechanisms between tools and workpiece materials during the cutting simulation process. The mean square displacement method was used to describe the diffusion process of workpiece atoms in SiC accurately.

In the present work, there are a large number of gaps in the nickel matrix composites at the nanoscale and the strengthening mechanism of the particle reinforcement on the nickel matrix at the nanoscale are still unclear. To explore the nanoscale wear properties of TiC/Ni composites, the effects of various parameters such as friction force, friction coefficient, wear scar depth and morphology, atomic displacement, and temperature are investigated in depth. The results obtained will help in the further application of TiC/Ni composites. This study is the first to establish an MD model of nickel-based composites containing TiC reinforcement, to simulate the microscopic friction and wear behaviors of nickel-based composites under repeated friction processes. This is also the first systematic study on the effects of TiC reinforcement on nickel-based composites during repeated friction processes. The strengthening mechanisms of TiC reinforcement in Ni-based materials during repeated friction processes were systematically studied and the essence of various friction and wear characteristics in Ni-based composites was revealed, which lays the foundation for the microscopic study of the effects of particle reinforcement on matrices.

2 Methods

2.1 Simulation modeling

In this study, repeated friction processes on TiC/Ni composites were studied using an MD method. As shown in Fig. 1, the proposed models include diamond grinding balls and TiC/Ni composites. The diameter of the grinding balls was 60 Å. Because the hardness of a diamond grinding ball is

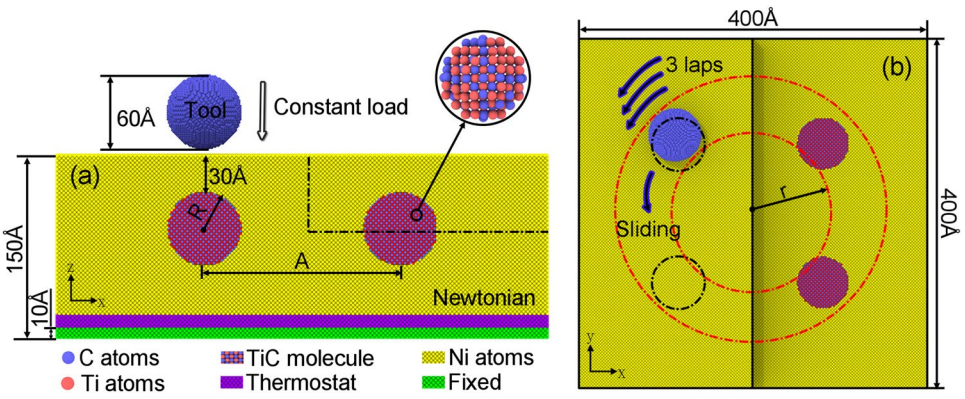

Fig. 1 Geometrical characteristics of a TiC/Ni sample from the (**a**) front and (**b**) top views

Table 1 Calculation parameters for MD friction simulations

Materials	Workpiece	Tool: Diamond
Dimensions	Cubic: 40 × 40 × 15 nm	Spherical: R = 3 nm
Atomic number	2184288	20112
Interatomic potential	MEAM/c EAM Morse	Tersoff
Time step	1 fs	
Initial temperature	300 K	
Grinding velocity	100 m/s	
Normal load	66 nN	
Grinding radius	11.3 nm	

much higher than that of a TiC/Ni composite, the grinding balls deform negligibly during the friction process. Additionally, this study mainly focused on the friction and wear behavior of the TiC/Ni composite, so the grinding ball was largely ignored. The TiC/Ni composite material is composed of a pure nickel phase and TiC phase, as shown in Fig. 1a. Four spherical TiC phases are uniformly distributed in the nickel matrix with a radius R of 30 Å and a distance of 30 Å from the workpiece surface. The distance between the TiC phases is 160 Å. In our simulations, the grinding ball performed periodic rotating friction events on the workpiece under a fixed load and constant rotation speed, which accurately reflects the characteristics of repeated friction on a workpiece under actual working conditions. This is an established scientific testing method for studying the friction and wear of materials [32], where the grinding ball rotation radius r is 113 Å and its movement direction is indicated by the blue arrow in Fig. 1b. Based on this model, the repeated friction behavior of a nickel-based alloy containing a carbide phase can be studied.

Table 1 lists the parameters selected for simulation. The size of the workpiece is 400 × 400 × 150 Å and it contains 2.18 million atoms, of which 2,141,697 are Ni atoms and 42,591 are TiC atoms. The workpiece atoms are divided into three zones: the uppermost yellow atoms represent the Newtonian layer, the middle purple atoms represent the thermostat layer, and the lowermost green atoms represent the boundary layer. The boundary layer is 10 Å thick and prevents the movement of the workpiece during the friction processes [33]. The constant-temperature layer is 10 Å thick and the temperature is maintained at 300 K by periodically adjusting the atomic velocity. The rest of the atoms are Newtonian layers, which follow Newton's second law and define the important region for studying material deformation and damage [30]. Additionally, to reduce the influence of boundary effects on simulation results, periodic boundaries are used in the x- and y-directions, and free boundaries are used in the z-direction [18, 30, 33]. Additionally, the conjugate gradient method is used for energy minimization to eliminate unreasonable factors for model building, such as atomic overlap.

2.2 Selection of potential function

To describe the interactions between different atoms, the neighborhood-modified embedded atom method (MEAM potential), atomic embedded potential (EAM potential), Tersoff potential, and Morse potential (Morse) were used in this study. MEAM (second-nearest-neighbor modified embedded atom method) was used to describe the interaction forces between Ti–Ti, Ti–C, and Ti–Ni in the composite. The total energy of the system E is defined as follows [16, 34, 35]:

$$E = \sum_i \left\{ F_i(\rho_i) + \frac{1}{2} \sum_{i \neq j} S_{ij} \emptyset_{ij}(r_{ij}) \right\}, \quad (1)$$

where F_i is the embedding energy for atom i embedded in a background electron density ρ_i, S_{ij} is the screening function, $\emptyset_{ij}(r_{ij})$ is the pair interaction between atoms i and j, and r_{ij} is the distance between atoms i and j.

EAM is the two-body potential [31] used in metal and alloy systems to describe Ni–Ni interaction forces. The total potential energy is expressed as follows [28, 36]:

Table 2 Parameter settings for the Morse potential function

Atomic type	Cohesion energy D	Elastic modulus α	Equilibrium distance r_0
C–Ni	0.100 eV	2.2 Å^{-1}	2.4 Å

$$E_{\text{tot}} = \frac{1}{2}\sum_{ij}\phi_{ij}(r_{ij}) + \sum_{i}F_i(\rho_i), \tag{2}$$

$$\rho_i = \sum_{j\neq i}\rho_j(r_{ij}), \tag{3}$$

where F_i is the embedded potential energy of atom i, ρ_i is the electron cloud density of the other atoms, $\varnothing_{ij}$ is the interatomic pair potential, and r_{ij} is the interatomic distance.

The Morse potential is used to describe the forces between C and Ni atoms and is defined in (4) [37].

$$U_{\text{Morse}}(r_{ij}) = D[\mathrm{e}^{-2\alpha(r_{ij}-r_0)} - 2\mathrm{e}^{-\alpha(r_{ij}-r_0)}]. \tag{4}$$

Here, D, r_0, and r_{ij} are the cohesive energy of exchange interactions, equilibrium distance, and separation distance between atoms i and j, respectively, and α is the bulk modulus fitted to the material. Table 2 lists the corresponding potential energy parameters.

Tersoff is used to describe the forces between C–C atoms in diamond tools and the interatomic energy is given by (5) [38].

$$\begin{aligned} E &= \frac{1}{2}\sum\nolimits_i\sum\nolimits_{j\neq 1}V_{ij} \\ V_{ij} &= f_C(r_{ij})\left[f_R(r_{ij}) + b_{ij}f_A(r_{ij})\right]. \end{aligned} \tag{5}$$

Here, the interatomic potential energy is V_{ij}, phase radius is f_c (r_{ij}), pair potential for mutual attraction between atoms is f_R (r_{ij}), modulation function is b_{ij}, and atomic spacing is r_{ij}.

3 Results and discussion

3.1 Study on the mechanical properties and wear trace morphology of the workpiece

To ensure that our simulation results were valid and accurate, the workpiece was relaxed before friction began, using the canonical ensemble (NVT) and the temperature was set to 300 K. The time step was 1 fs to ensure authenticity and stability of the system [39]. The friction process used a micro-canonical ensemble (NVE). Because the system energy balance is the result of the atomic self-adjustment of the equilibrium position, changes in the system energy are closely related to the adjustment of atom displacement.

Figure 2 presents the variation in the atomic displacement deformation and total energy of the workpiece, with the aforementioned time step during the relaxation process. One can see that the total energy increases sharply with the number of steps at the beginning of relaxation and after reaching the highest point, the total energy tends to stabilize and fluctuate slightly. During relaxation, the matrix Ni atoms first shift and their color changes to light green, whereas the TiC phase atoms do not shift and their color is blue, as shown in Fig. 2a. As the number of relaxation steps increases, the total energy gradually increases. The matrix atoms transfer their displacement to the TiC phase through interactions, such that the TiC phase atoms shift as well and their color changes to orange-yellow, as shown in Fig. 2c. When the energy of the system reaches its maximum and tends to stabilize, all the atoms except those in the fixed boundary undergo large displacement under deformation adjustment and the overall color becomes red, as shown in Fig. 2e. Thereafter, the system reaches equilibrium and the energy only fluctuates slightly, and there are no large displacements in the workpiece atoms.

To accurately study the force changes of the grinding ball in the X- and Y-directions during the entire friction process, the forces between the grinding ball and workpiece were extracted, as shown in Fig. 3. One can see that F_x and F_y vary periodically according to sine and cosine curves, respectively. The main reason for these fluctuations is the plastic deformation that occurs during the friction process. In the figure, a, b, and c, and a', b', and c' represent the valley and peak values of F_y in the first, second, and third friction processes, respectively. One can see that the absolute values of a and a' are greater than those of b and b', indicating that the absolute values of the peak and valley values

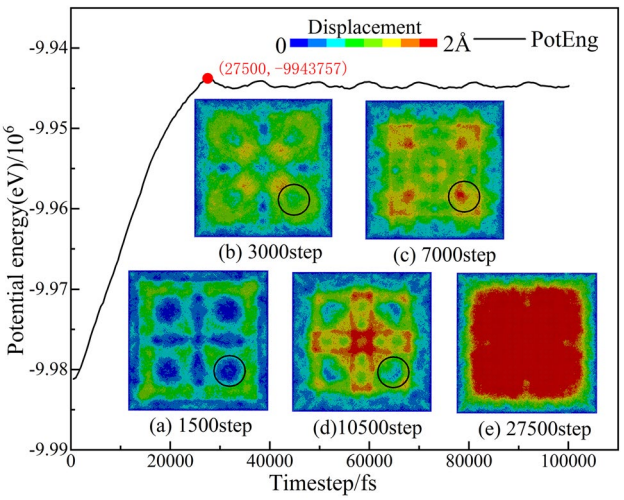

Fig. 2 Effects of relaxation of the workpiece on changes in the atomic displacement and total energy of the workpiece

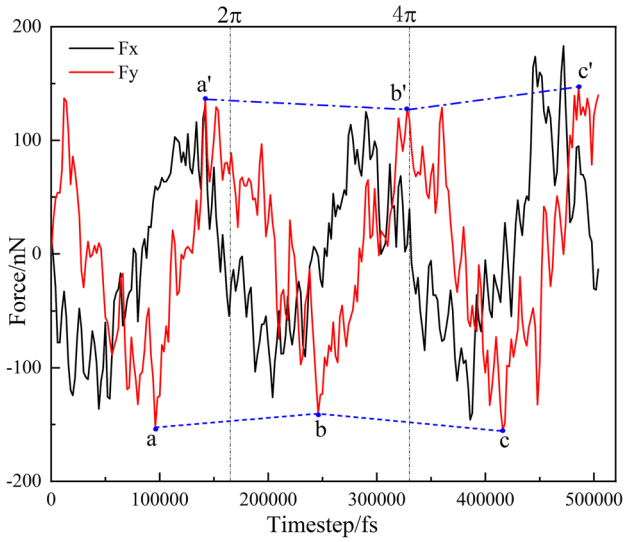

Fig. 3 Interaction between the grinding ball and workpiece in the *X* and *Y* directions

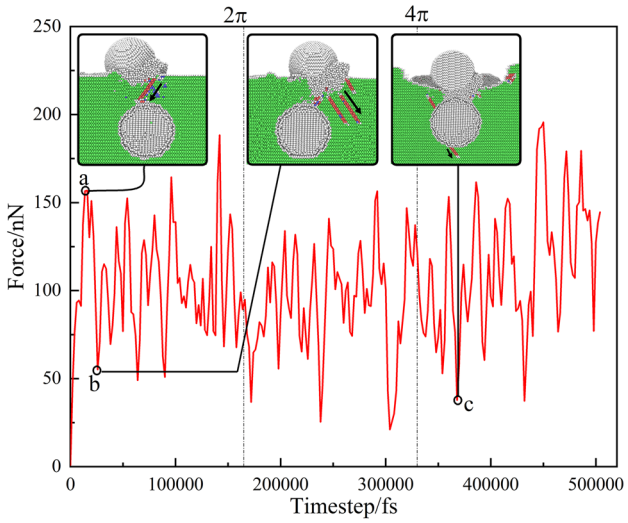

Fig. 4 Dynamic friction response curve with advancing time steps

for the initial friction process are greater than the absolute values of the corresponding peak and valley values for the secondary friction process. This is because the surface of the workpiece is relatively intact at the time of initial friction, so it produces more atoms in the form of abrasive chips, and thus more resistance to the grinding ball. However, the absolute values of b and b' are smaller than the absolute values of c and c', indicating that the Y-directional friction component of the secondary process friction is smaller than that of the tertiary friction process. This is because, as the number of friction processes increases, the position of the grinding ball gradually moves downward and the distance to the TiC phase decreases, but the hardness of TiC is relatively high, which causes the resistance to the grinding ball to increase. This indicates that as the number of friction processes increases, the strengthening effect of TiC on the workpiece gradually increases.

To accurately study the relationship between the change in friction and deformation of the material, the friction components can be combined to obtain the resultant friction force F_f, as shown in formula (6).

$$F_f = \sqrt{(F_x)^2 + (F_y)^2} \tag{6}$$

Here, F_f is the frictional force, the X-directional force is F_x, and the Y-directional force is F_y.

Figure 4 presents the dynamic response curve of the friction force with advancing time steps. One can see that the defect at the lower end of the grinding ball nucleates and develops toward the inside of the workpiece. When the defect is blocked by the TiC phase, a tendency to extend inward is prevented and the energy cannot be released through the extension and development of defects, resulting in energy accumulation in the action area, which leads to increased friction force. With the continuous action of the grinding ball on the workpiece, the frictional force reaches an extreme value, as shown at point "*a*" in Fig. 4. When the grinding ball passes through the TiC phase, the friction force decreases sharply and a minimum value appears at point "*b*." This is because the defects at the lower end of the grinding ball can be completely extended and developed inside the workpiece at this time, and the accumulation energy of the grinding ball on the workpiece can be fully released, which leads to a reduction in the friction force.

Additionally, after experiencing two friction processes, the frictional force at point "*c*" also exhibits an extreme minimum value. This can be attributed to the relatively stable structure of TiC atoms, which prevents defects from extending toward the inside of the workpiece, so the energy cannot be fully released. However, the energy passes through the TiC phase, causing the nucleation and development of defects below the TiC phase; the energy is released and the frictional force exhibits a minimum value. This indicates that there is a blocking effect on the motion of the grinding ball at the interface between the pure nickel phase and the TiC phase, and that the large fluctuations in friction force are caused by the accumulation and release of energy at this interface.

The coefficient of friction can reflect the frictional properties of the material and is defined as follows [7]:

$$\mu = F_f / F_z, \tag{7}$$

where μ is the coefficient of friction, F_f is the frictional force, and F_z is the Z-directional force.

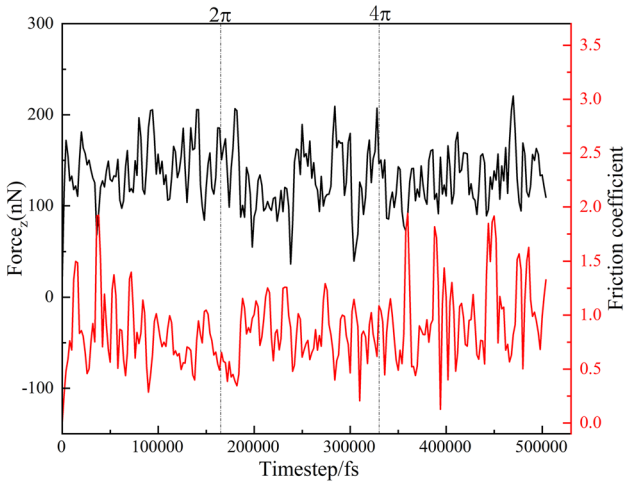

Fig. 5 Dynamic response curves of the force and friction coefficient with advancing time steps in the *Z*-direction

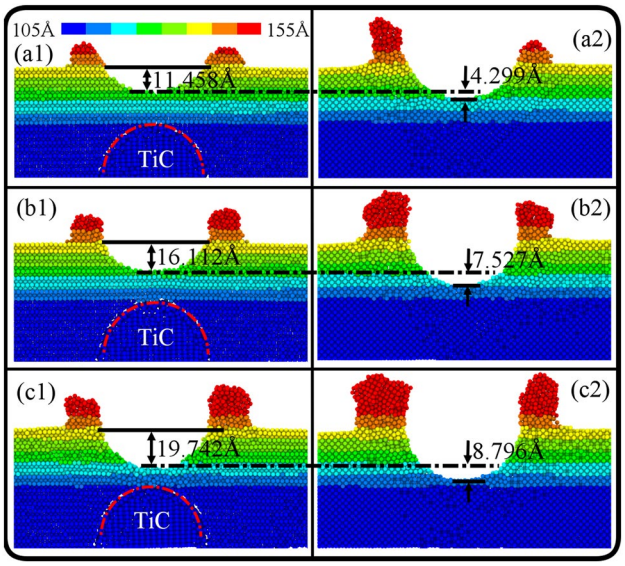

Fig. 6 Wear scar morphology after different numbers of friction processes: (**a**) first process, (**b**) second process, and (**c**) third process

Figure 5 presents the variation in the force F_z and friction coefficient between the grinding ball and workpiece atoms in the *Z*-direction, with advancing time steps. As the grinding ball is rubbed under a fixed load throughout the friction processes, F_z fluctuates up and down around the equilibrium position. The main reason for this fluctuation is the plastic deformation of the material during friction and the presence of TiC.

At the beginning of friction, the value of the friction coefficient changes significantly because the surface of the workpiece is not damaged and the surface quality is excellent. Entering the secondary friction, the friction coefficient peaks near the TiC phase. This is due to the strengthening effect of the two-phase interface on the workpiece atoms, and the wear rate has a certain periodic peak around the relative position of the TiC phase. When the grinding ball reaches the third circle, the friction coefficient fluctuates greatly, and a large peak appears near the TiC phase. Therefore, the change of the friction coefficient is closely related to the relative position of the TiC phase. The closer the grinding ball is to the TiC phase, the more obvious the strengthening effect of the TiC phase.

Figure 6 presents the atomic Z-directional height of three friction troughs with depth of color calibration to highlight the wear depths and morphologies of different numbers of friction processes. In Fig. 6a1–c1 shows the grinding ball on the TiC phase the morphologies of the wear marks the grinding ball on the TiC phase, and (a2), (b2), and (c2) show the morphologies of the grinding ball on the non-TiC phase. By comparing (a1) to (a2), (b1) to (b2), and (c1) to (c2), one can see that the depth of the abrasion marks is shallower with the same number of turns with the TiC phase than without the TiC phase. The differences between the two are 4.299 Å, 7.527 Å, and 8.796 Å for the first, second, and third identical friction processes, respectively. This is a result of the interfacial effect that exists between the TiC phase and substrate, which prevents the continuous removal of material and results in differences in the depth of the abrasion marks. By comparing the abrasion depths between (a1), (b1), and (c1), and (a2), (b2), and (c2), one can see that the differences in abrasion depth at different numbers of turns become smaller as the number of friction processes increases. When the grinding ball is located above the TiC phase, the depths of the wear marks in the first, second, and third turns are 11.458 Å, 16.112 Å, and 19.742 Å, respectively. This is because repeated friction processes lead to the hardening of the friction surface, causing the wear mark differences to decrease.

A detailed analysis of the depth of the abrasion marks at each friction moment is presented in Fig. 7. One can see that the variation in the depth of the initial friction marks is small and it fluctuates relatively sharply. This is a result of the drastic plastic deformation that occurs inside the workpiece during the initial friction processes, which make changes in the depth of the abrasion marks more frequent. As the number of friction processes increases, the variation range of the wear scar depth increases, the peak and valley values alternate with each other, the difference between the peak and valley values becomes larger, and the peak value mainly appears near the TiC phase, as shown in Fig. 7 for Δh_1, Δh_2, and Δh_3. This indicates that the TiC phase has a strengthening effect and the closer the grinding ball is to the TiC phase, the more apparent is the strengthening effect.

During the friction processes, the wear rate can be calculated from the volume of the workpiece atoms removed by

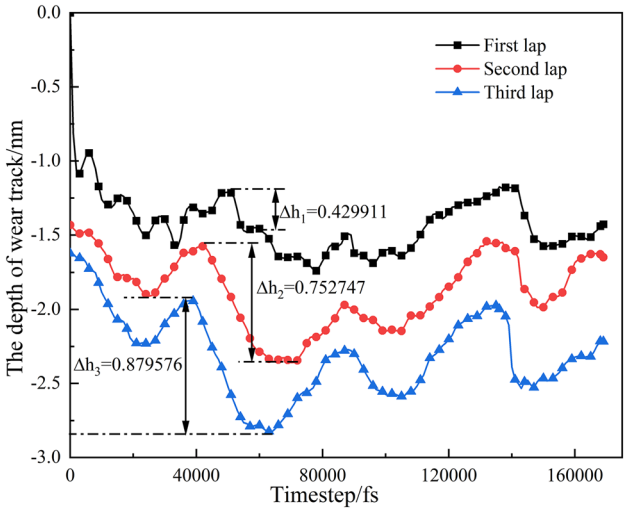

Fig. 7 Dynamic response curves of wear scar depth with continuous friction processes

the grinding ball. Figure 8 presents a schematic diagram of the calculation of the wear volume, where the calculation of the wear volume is divided into volume calculations for the initial and repeated friction processes. Because the depth of the abrasion marks did not exceed the radius of the grinding ball in our simulations, only cases in which the depth of the abrasion marks did not exceed the radius of the grinding ball were considered. Figure 8a presents the calculation of the first friction wear volume and Fig. 8b presents the calculation of the repeated friction chip volume. The instantaneous wear volume ΔV can be calculated based on the abrasion depth Δh, as shown in formula (8).

$$\Delta V = \int_{R-\Delta h}^{R} (\pi r^2) \mathrm{d}z. \tag{8}$$

Here, ΔV is the instantaneous wear volume, R is the radius of the grinding ball, and Δh is the depth of the wear marks.

With homogeneous materials, the relationship between the wear volume (V), normal load (F), and sliding distance (L) at the contact point follows the Archard equation [40].

$$V = \delta FL. \tag{9}$$

Here, δ is the instantaneous wear rate. The instantaneous wear rate formula is:

$$\delta = V/FL \tag{10}$$

where δ is the instantaneous wear rate, V is the wear volume, L is the sliding distance, and F is the normal load at the point of contact.

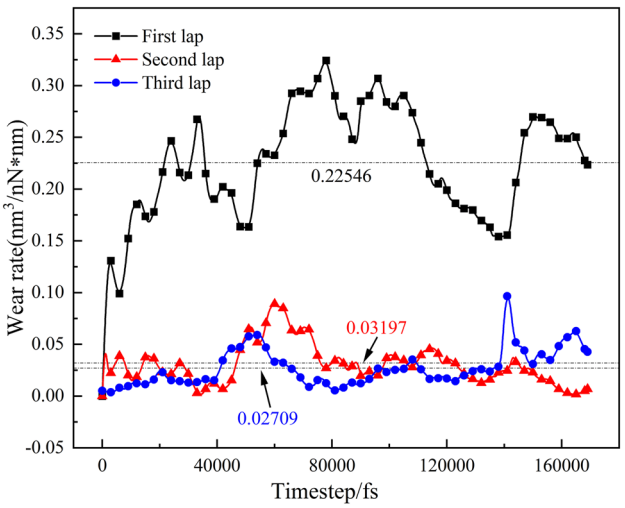

Fig. 9 Wear rate curves

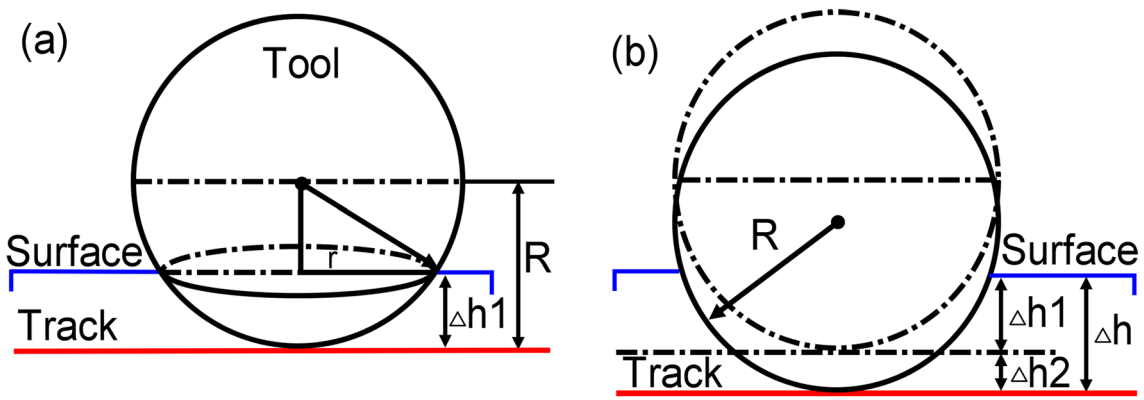

Fig. 8 Schematic diagrams of friction processes: (**a**) schematic diagram of primary friction and (**b**) schematic diagram of repeated friction

The wear rate reflects the wear of the material. By using formula (9), the change curve of the wear rate over time can be calculated, as shown in Fig. 9. One can see that the initial frictional wear rate is large and fluctuates significantly. Additionally, the fluctuations are mainly concentrated near the TiC phase, indicating that TiC has a strengthening effect relative to the nearby nickel atoms. However, in the repeated friction process, the average wear rate gradually decreases with the second and third lap wear rates being 0.03198 and 0.02709. It indicates that repeated friction leads to hardening of the friction surface, the grinding ball cannot remove more atoms, and the more the number of friction, the stronger the hardening of the material. Meanwhile, the peak of the wear rate appears, which is mainly related to the strengthening effect of the TiC phase, indicating that the change of the wear rate is closely related to the location of the TiC phase.

3.2 Effects of atomic displacement

To some extent, atomic displacement reflects the deformation of the material. Atomic displacement can be color-calibrated according to its magnitude during friction processes, as shown in Fig. 10. In Fig. 10a, one can see that when the grinding ball touches the atoms of the workpiece and is not in contact with the TiC, and the number of atoms displaced in the entire workpiece is high. However, neither TiC nor its neighboring Ni atoms are displaced. This indicates that the presence of the TiC phase hinders the deformation of the workpiece. However, when the grinding ball rubs directly above the TiC, only the front end of the grinding ball and the workpiece atoms, in the area being ground, are displaced, as shown in Fig. 10b. This is because the TiC as a whole withstands the action of the grinding ball on the workpiece, meaning no extensive deformation of the workpiece occurs. As the grinding ball continues to press down and rotate, and as it moves closer to the TiC phase, the number of displaced workpiece atoms increases again and the range of workpiece deformation increases, but the TiC and nearby atoms remain in place, as shown in Fig. 10c. Again, when the grinding ball rubs on the TiC, only the front-end of the grinding ball and the atoms in the workpiece being ground are displaced, as shown in Fig. 10d.

After the first friction process, repeated friction processes were performed on the friction surface, as shown in Fig. 10e, f. We determined that the change trend in the atomic displacement of the workpiece was the same as that during the initial friction process. The deformation hindrance of the workpiece and the ability of the TiC to bear the action of the grinding ball still exist in the repeated friction processes.

To accurately analyze the deformation law of the workpiece during friction and eliminate the effects of small displacements of atoms caused by excitation, temperature, etc., the number of atoms with displacements greater than 1.8 Å during the friction processes was counted, as shown

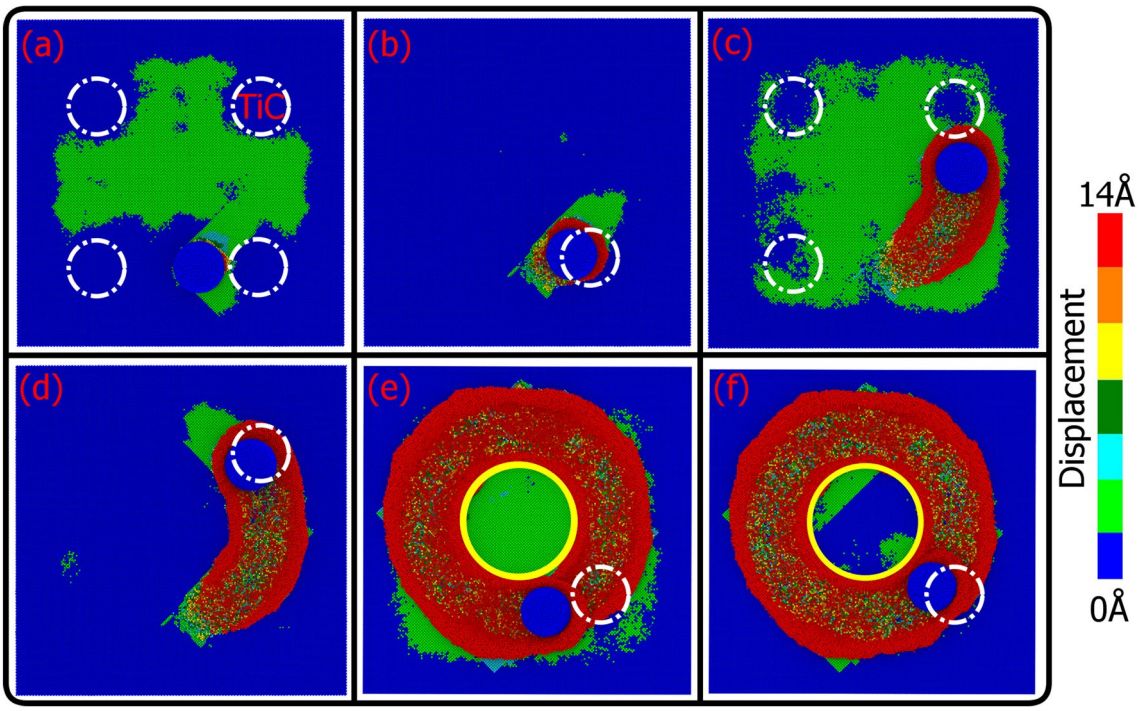

Fig. 10 Changes in atoms with displacement greater than 1.8 Å during friction processes. (**a**–**f**) represent the friction morphologies at different times

in Fig. 11. The red line represents the number of internally displaced atoms in the workpiece when the grinding ball is not in contact with the TiC (e.g., moments a, c, e) and when it is in contact with the TiC (e.g., moments b, d, f). The blue line was obtained by counting the average number of displaced atoms inside the workpiece, when the grinding ball was in contact with the TiC and when it was not. By analyzing the average slope of the displaced atom numbers, we found that the number of atoms displaced during the friction processes continued to increase and that the growth rate $\Delta\delta_1$ of the number of displaced atoms during the initial friction process was greater than the growth rates $\Delta\delta_2$ and $\Delta\delta_3$ during the repeated friction processes. This indicates that in the initial friction process, the number of displaced atoms increases rapidly and the grinding ball has a large range of action on the workpiece, whereas in the repeated friction processes, the number of displaced atoms increases slowly and the range of action of the grinding ball on the workpiece is relatively small. The main reason for this is that in the initial friction process, there is no damage inside the workpiece and the deformation can be transmitted to the entire workpiece through the interaction between atoms. In the repeated friction processes, the hardening of the rubbed surface and defects in the subsurface prevent the transfer of interactions between atoms, so the scope of action of the grinding ball on the workpiece is reduced. The moments of *a*, *b*, *c*, *d*, *e*, and *f* in Fig. 11 correspond to those shown in Fig. 10, where one can see that during the initial friction process, the number of atoms displaced is high when the grinding ball is not in contact with the TiC and low when it is in contact with the TiC. This phenomenon is repeated during repeated friction processes.

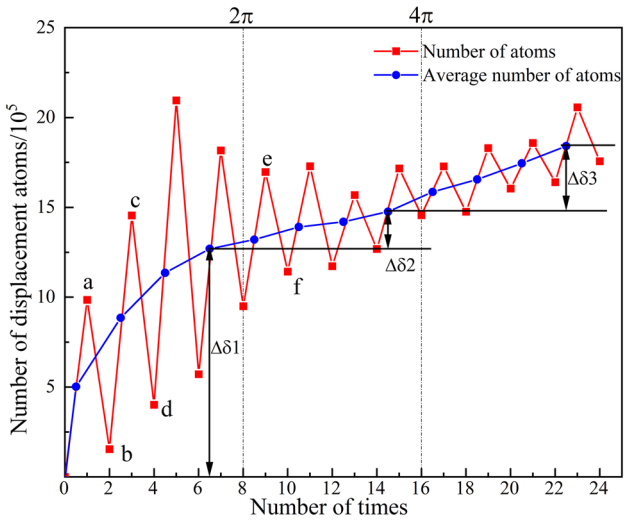

Fig. 11 Changes in the number of atoms with displacements greater than the 1.8 Å in the form of a dynamic step response curve

To clearly interpret the deformation behavior of the workpiece during the friction processes, an atomic displacement vector change diagram was obtained, as shown in Fig. 12. When the grinding ball acts on the nickel substrate away from the TiC phase, the atoms above the grinding ball move obliquely upward under the friction and extrusion of the grinding ball, and eventually become wear debris. The atoms below the grinding ball move toward the inside of the workpiece and the direction of friction relative to the displacement trend is 45°, as shown in Fig. 12a. This is because the target of the grinding ball action is single-crystal Ni with a face-centered cubic (FCC) structure, which is prone to

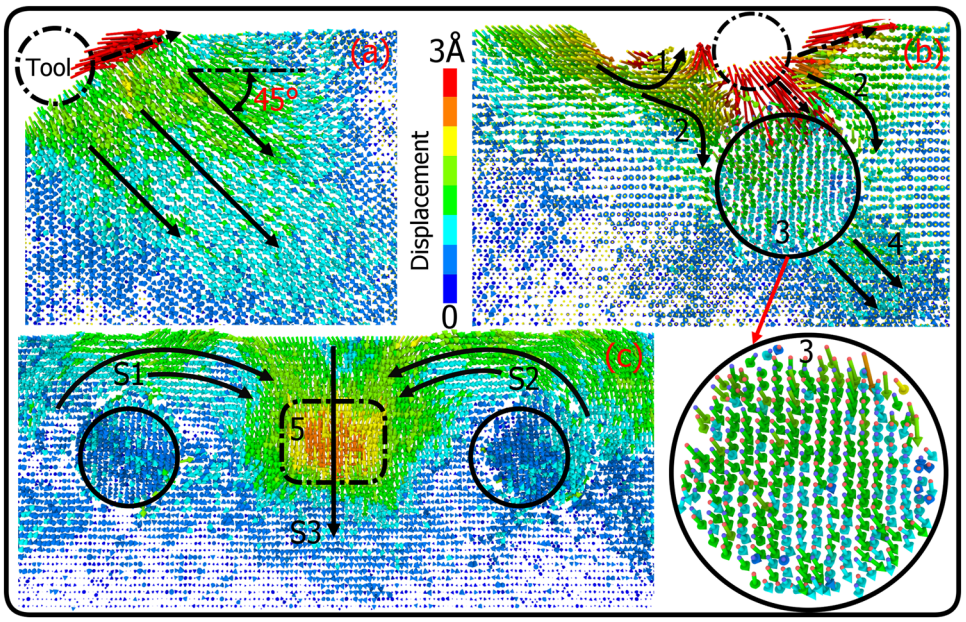

Fig. 12 Different position displacement vector displays; (**a**) the grinding ball acts on the nickel substrate away from the TiC phase; (**b**) the grinding ball rubs near the TiC phase; (**c**) the grinding ball is located at the far-end of the TiC phase

displacement along its plane of slip when subjected to external action. When the grinding ball rubs near the TiC phase, an elastic recovery of the atoms behind the grinding ball occurs based on the departure of the grinding ball, producing an upward displacement vector, as shown in Fig. 12(b)1. The matrix atoms below the grinding ball are hindered by the TiC phase during their movement toward the interior of the workpiece. As the action energy of the grinding ball on this portion of the matrix atoms continues to increase, the action of the atoms on the TiC phase also increases. Based on the high hardness of the TiC phase, the atoms are unable to break through the TiC phase and continue their movement in their original direction, so the direction of displacement is deflected and begins to extend toward the interior of the workpiece along both sides of the TiC phase, as shown in Fig. 12(b)2. Noticeable hindrance of SiC particles was also observed by Xu et al. [41] when cutting SiC/Al-NCs. It is important to note that at this time, the matrix atoms still have a strong effect on the TiC phase, so the TiC phase as a whole produces a small downward displacement, as shown in Fig. 12(b)3. When the effect of the TiC phase is sufficiently large, it is transferred to the matrix atoms on the lower side, causing those atoms to move away from the original lattice points, as shown in Fig. 12(b)4.

When the grinding ball is located at the far-end of the TiC phase, the action of the grinding ball on the workpiece causes the matrix atoms to bypass the TiC phase and move along the *S1* and *S2* directions. After the two sets of atoms with opposite vectors intersect in the middle of the workpiece, they produce a downward displacement trend *S3*, as shown in Fig. 12c. Because *S3* is the result of the intersection of the *S1* and *S2* vectors, the displacement is numerically larger and has an orange color, as shown in Fig. 12(c)5.

3.3 Variation of internal defects with friction processes

Figure 13 presents the distribution of dislocations in the workpiece during the friction processes. In this study, dislocations were identified using the dislocation extraction algorithm [42] in OVITO.

Previous studies have demonstrated that for metal matrix composites, a semi-coherent interface forms between the matrix and inclusions when the lattice mismatch exceeds 5% [43]. This also occurs in TiC/Ni matrices, where the lattice mismatch is calculated as follows:

$$\delta = \frac{a_N - a_S}{a_N}, \tag{11}$$

where a_N is the TiC atomic lattice constant and a_S is the nickel atomic lattice constant. According to the relevant literature, the TiC atomic lattice constant is 4.33 [44] and the nickel atomic lattice constant is 3.52 [45]. The mismatch of the lattice in the TiC/Ni matrix is approximately 18%.

As shown in Fig. 13a, during the initial friction process, the material is plastically deformed when the grinding ball first touches the workpiece surface, generating many Shockley partial dislocations with a Burgers vector of 1/6 ⟨112⟩ that extends as far as the workpiece surface or the TiC phase. Additionally, a few Shockley dislocations occur on the TiC surface, which are isolated into "u-shaped" dislocations and ringed on the TiC phase surface, as shown in Fig. 13(a)1. Under the continuous action of the grinding ball on the workpiece, the TiC phase blocks the further growth of dislocations along the slip system, resulting in a large number of dislocations between the grinding ball and TiC phase, as shown in Fig. 13(b)2. When the dislocation extension is blocked, friction hardening eventually occurs. Moreover,

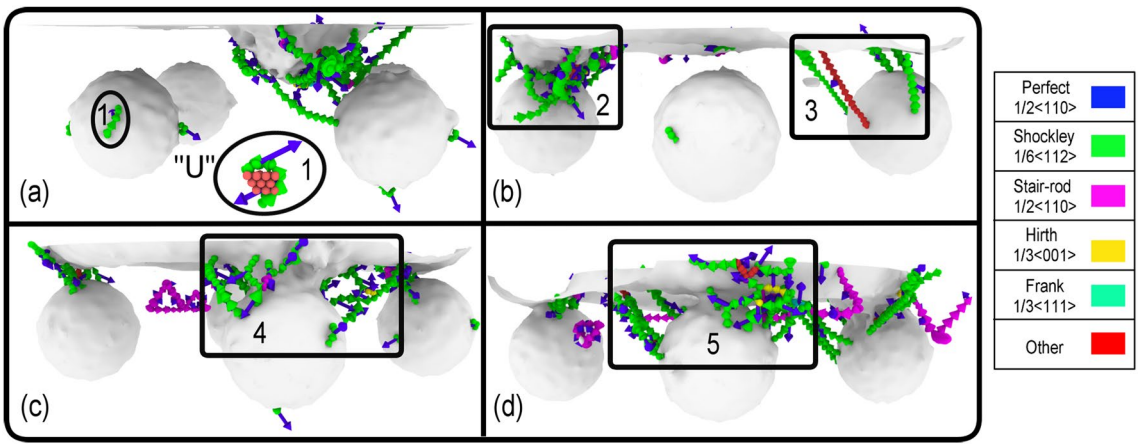

Fig. 13 Evolution of dislocations in a TiC/Ni workpiece. (**a**) The grinding ball just touches the workpiece surface. (**b–d**) Grinding ball friction at the first, second, and third positions on the same TiC workpiece

Ni–Cu interface [37], Al–Si interface [46], grain boundary [47], stacking faults [48], etc., have also been observed in similar scenarios. Additionally, after the grinding ball leaves the area under grinding, the number of dislocations between the grinding ball and TiC phase decreases as a result of elastic recovery, marking a transition from agglomerate dislocations to linear dislocations, as shown in Fig. 13(b)3.

When entering the repetitive friction stage, as the friction increases, the action energy between the grinding ball and TiC phase continues to increase with an increasing number of dislocations, as shown in Figs. 13(c)4 and (d)5. This indicates that as the number of friction processes increases, dislocation continues to increase and dislocation entanglement is generated, leading to friction hardening and improving the deformation resistance of the workpiece. Additionally, stair-rod dislocations are present throughout the friction process, which mainly connects the two Shockley dislocations and extend to the workpiece surface to form a stable structure.

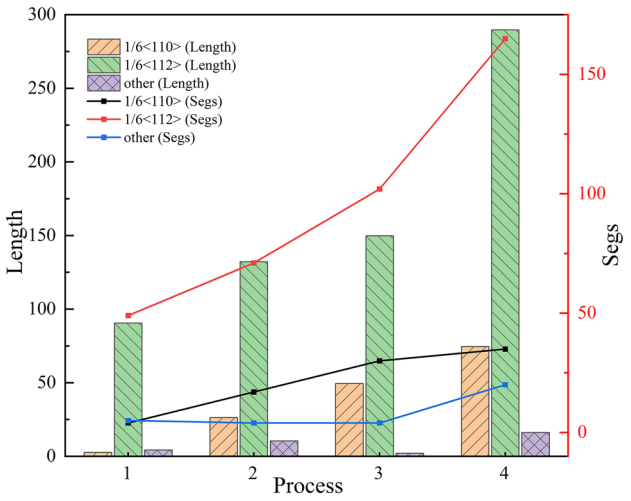

Fig. 14 Statistics on the length and number of dislocations in different positions

The number and length of the stair-rod, Shockley, and other dislocations in the first friction process, repeated friction processes, and when the grinding ball just touches the workpiece, were counted to accurately analyze the dislocation distribution law during friction, as shown in Fig. 14. Moments 1, 2, 3, and 4 in Fig. 14 correspond to moments a, b, c, and d in Fig. 13. One can see that as the number of friction processes increases, the length and number of dislocations increase. Considering the results in Fig. 13, this further verifies that repeated friction processes are prone to forming dislocation entanglements, which eventually leads to friction hardening.

In this study, defect analysis of the workpiece surface during three friction processes was conducted, as shown in Fig. 15. The common neighbor analysis method was used to color different types of atoms, and the nickel atoms in the intact FCC structure were removed. The atoms with the hexagonal close-packed (HCP) structure were colored red, the atoms of the body-centered cubic (BCC) structure were colored blue, the amorphous atoms were colored white, and the stacking faults were represented by two layers of red atoms. As shown in Fig. 15a, in the initial friction process,

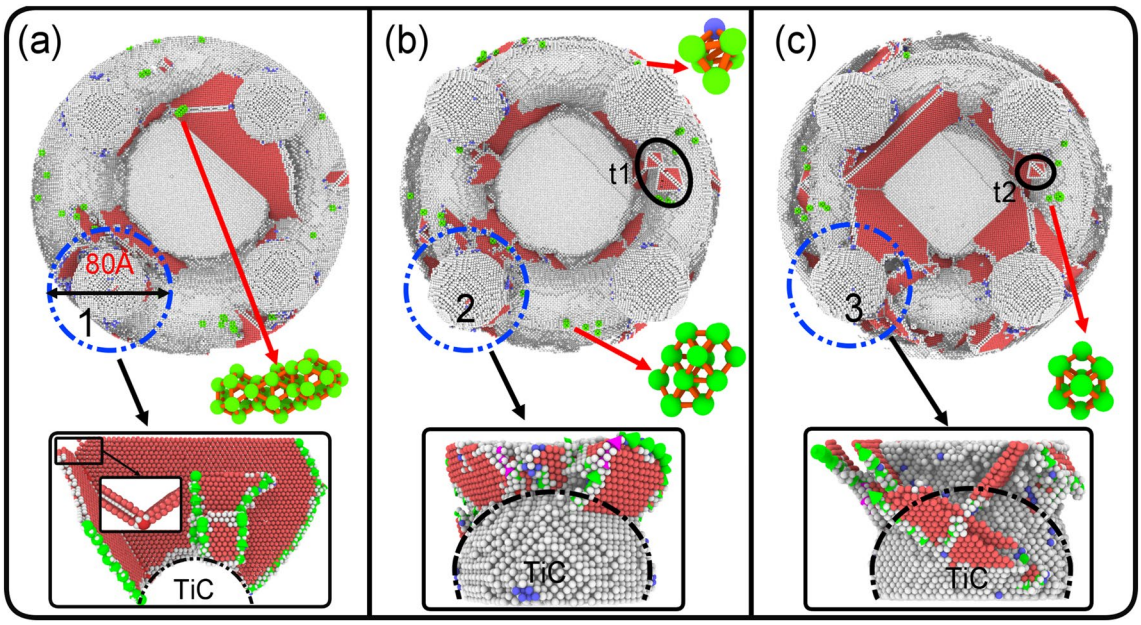

Fig. 15 Types of defects in the workpiece under different friction processes. The green atoms represent atomic clusters. Numbers 1, 2, 3 highlight schematic diagrams of defects near the TiC phase in each friction ring

the defect distribution is uneven, large structural defects are generated between the TiC phase and the surface of the workpiece, and the extension of defects is hindered by the TiC phase, which makes it difficult to produce large structural defects below the TiC phase, thereby protecting the internal matrix. It should be noted that the structure dominated by large structural defects around the TiC phase, as shown in Fig. 15(a)1. When entering the second friction process, the large structural defects generated by the initial friction process fail to form a stable structure, evolve under the continuous extrusion of the grinding ball and decompose into smaller defects, such as clusters of atoms and amorphous atoms, as well as relatively stable a stacking fault-like tetrahedral structure, as denoted by "t1" in Fig. 15b. At this point, the defects around the TiC phase are numerous and mainly in the form of small layer faults, as in Fig. 15(b)2. When entering the third friction process, as the distance between the grinding ball and TiC phase shrinks, the force on the TiC phase increases. Therefore, a portion of the defect structure above the TiC phase is decomposed into an amorphous structure under the extrusion of the grinding ball and large structural defects occur in the middle part of the TiC phase, as shown in Fig. 15(c)3. Simultaneously, more defects appear inside the workpiece and form a new structure of a whole, which leads to the improved stability of the internal material of the workpiece, as shown in Fig. 15c. Additionally, repeated friction processes cause the relatively stable laminar dislocation tetrahedral-like structure to evolve into a more stable laminar dislocation tetrahedral-like structure, as denoted by "t2" in Fig. 15c.

To accurately analyze the dislocation distribution law between the grinding ball and TiC phase during the friction process, at positions 1, 2, and 3 in Fig. 15 the length and total number of stair-rod, Shockley, and other dislocations in a sphere with the TiC center as the sphere center and diameter of 80 Å was counted, as shown in Fig. 16. One can see that the total number of dislocations gradually increases with the number of friction processes and the lengths of the stair-rod, Shockley, and other dislocations vary less in the first and second processes, but elongate significantly in the third process, which can be attributed to the reduced distance between the grinding ball and TiC phase. The results discussed above further indicate that as the number of friction processes increases, dislocation plugging is more likely to occur near the TiC phase, making the material less easy to remove and leading to a reduction in the wear rate.

To describe variations in the regular pattern of defect atoms inside the workpiece, the number of defect atoms was partially counted, as shown in Fig. 17. Figure 17a presents a statistical plot of the numbers of atoms with BCC, HCP, and amorphous structures during the friction process. One can see that the atomic numbers of the HCP structures and other structures increase rapidly during the initial friction process,

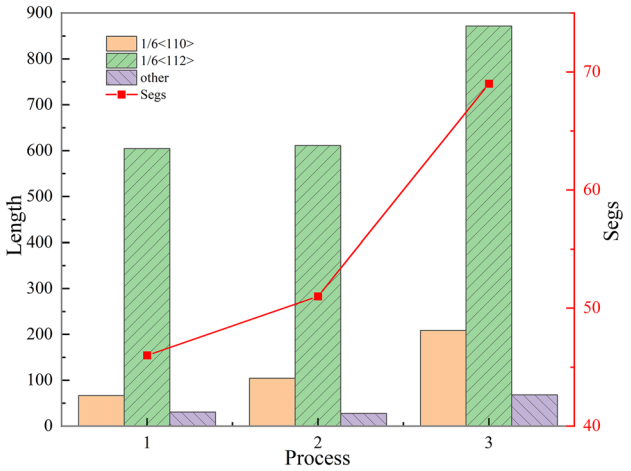

Fig. 16 Statistics for different winding numbers, lengths, and numbers of dislocations in the same position

based on the large number of abrasive chips and dislocations generated during the initial friction process, which causes the atomic number of the other structures to increase faster, while the rapid increase in the atomic number of the HCP structures can be attributed to the energy generated by the continuous squeezing of the grinding ball on the workpiece, which is released in the form of dislocations. When entering the second friction process, the increase in the atomic number of the other structures slows as a result of the hardening of the friction surface by the initial friction process, which makes it more difficult to remove material during subsequent friction processes, thereby lowering the production of abrasive debris, resulting in a slower increase in the atomic number. Large fluctuations in the HCP atoms occur because this stage is associated with the process of destroying the large structural defects produced by the initial friction process. The defects with HCP structures are squeezed or recovered. Upon entering the third friction process, the atomic numbers of the Other and HCP structures increase rapidly again as a result of the reduced distance between the grinding ball and TiC, which causes more atoms of the Other and HCP structures to be produced between the grinding ball and TiC. The atomic number of the BCC structures remains almost unchanged during the repeated friction processes.

Figure 17b presents a comparison of the total numbers of BCC, HCP, and amorphous structure atoms per friction process. One can see that the total number of atoms generated by the initial friction process is greater than the amount generated by continued friction processes. This is because the initial process removes more material and produces more defective atoms, resulting in a higher total number of atoms. The total number of atoms in the secondary friction process first increases and then decreases as a result of the rotating downward pressure of the grinding ball and removal of the

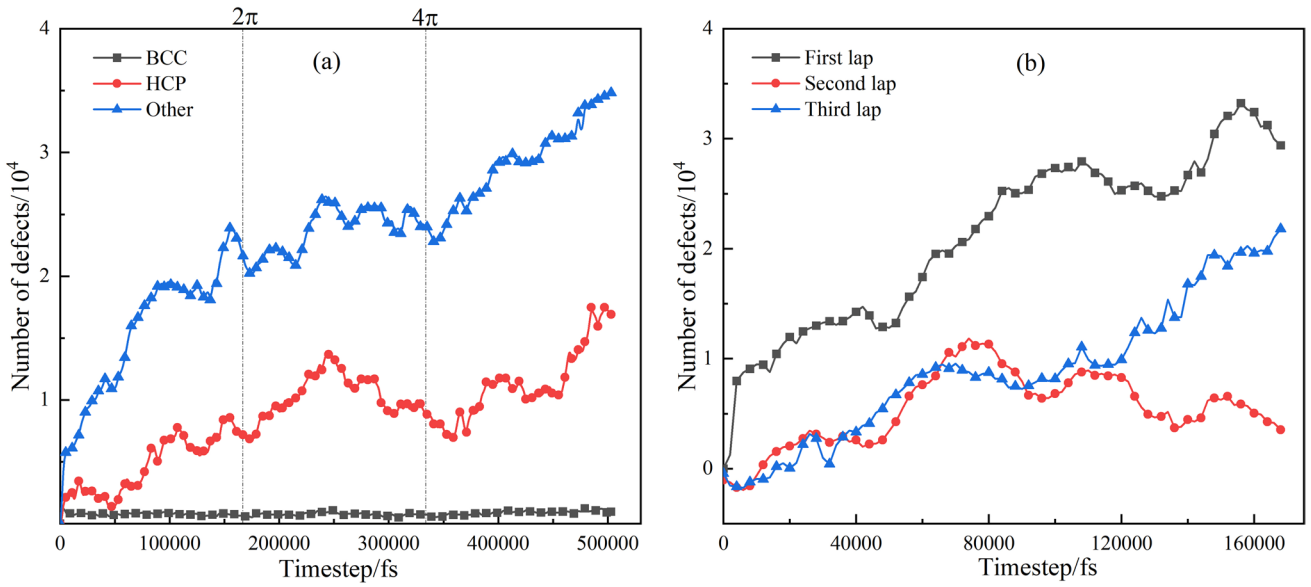

Fig. 17 Defect atomic number statistics; (**a**) Numbers of BCC, HCP, and other atoms during repeated friction processes and (**b**) comparison of the total number of defects per friction process

residual workpiece material from the initial friction process by the grinding ball at the beginning of the second friction process. The increase in the total number of atoms during the third process can be attributed to the fact that the distance between the grinding ball and TiC decreases, causing a large number of amorphous atoms to appear between them. Simultaneously, a large number of defective structures appear inside the workpiece, leading to an increase in the total number of atoms.

Figure 18 presents the evolution process of the formation and volume decrease of stacking fault tetrahedrons. According to the previous dislocation analysis, one can see that the Shockley dislocations continue to move and gradually begin to separate from the stair-rod dislocations, making the stair-rod dislocations appear independently and forming a complete stacking fault tetrahedron. As highlighted by labels in 1–4 in Fig. 18, two connected stacking fault tetrahedrons are first formed on the side with more atoms. These tetrahedrons release a large amount of energy during their formation process, separating them from other types of defective structures and eventually forming two connected tetrahedral structures. However, based on the continuous

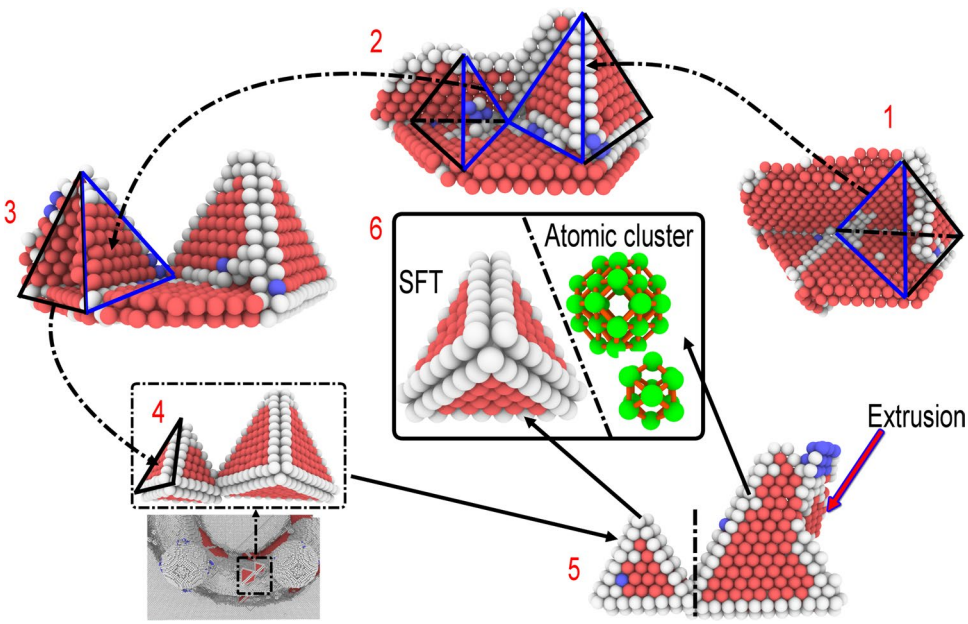

Fig. 18 Evolution process of the formation and volume reduction of stacking fault tetrahedrons. (*1–4*) Formation of stacking fault tetrahedrons, (*5*) extrusion process, and (*6*) stable stacking fault tetrahedron and atomic clusters.

squeezing of the workpiece by the grinding ball during friction processes, the structure of the larger stacking layer dislocation tetrahedron is disrupted and the dislocations first begin to extend from the apex of the tetrahedron, deviate from the original crystal position, and then continue to evolve, as shown in Fig. 18 (label 5). During this evolutionary process, interstitial atoms are continuously formed and they attract each other under the action of internal stress, and gradually aggregate to form atomic clusters. The smaller stacking fault tetrahedrons become stable and are separated to form a more stable stacking fault tetrahedron structure, as shown in Fig. 18 (label 6). The generation of stacking fault tetrahedrons reduces the energy of internal defects and forms stable defects in the workpiece, which ultimately leads to friction hardening [33].

3.4 Temperature change mechanisms during friction

Figure 19 presents the distribution of the atomic temperature of the workpiece with repeated friction processes. As shown in Fig. 19a, when the grinding ball reaches the vicinity of the TiC phase in the initial friction process, the high-temperature atoms are primarily grinding chips. However, the temperature of the TiC atoms is higher than the temperature of the nickel matrix atoms at the same height, as a result of the energy generated by the movement of defect and matrix atoms acting directly on the TiC phase. As shown in Fig. 19b, when the grinding ball comes near the TiC phase in secondary friction process, the temperature of the TiC phase is higher than the temperature in the initial friction process. This is a result of the increase in the number of friction processes, stronger action of the grinding ball on the TiC phase, additional defects acting directly on the TiC phase, and more intense movement of the matrix atoms around the TiC. However, the temperature of the matrix atoms at the same height is still lower than that of the TiC atoms. As shown in Fig. 19(c1), when the grinding ball rubs near the TiC phase for the third time, the TiC atoms are mainly dominated by high-temperature atoms. This is because the grinding ball destroys the defects between the TiC phase and itself, so the grinding ball has a stronger effect on the TiC. Additionally, there is only a small difference in hardness between the grinding ball and TiC atoms, which causes all of the TiC atoms to become high-temperature atoms. At the same time, the temperature of the atoms on the workpiece surface around the TiC is higher than the temperature of the atoms around the TiC-free zone, as shown in Fig. 19(c2)1. However, the temperature of the matrix atoms is still lower than that of the TiC atoms

The atomic temperatures at each of the three moments in Fig. 19a–c are extracted to analyze the temperature distribution rule, as shown in Fig. 20. One can see that with an increase in the number of friction processes, the temperature continuity between the base atoms and TiC degrades, as shown in Fig. 20 (label 1). This is attributed to the fact

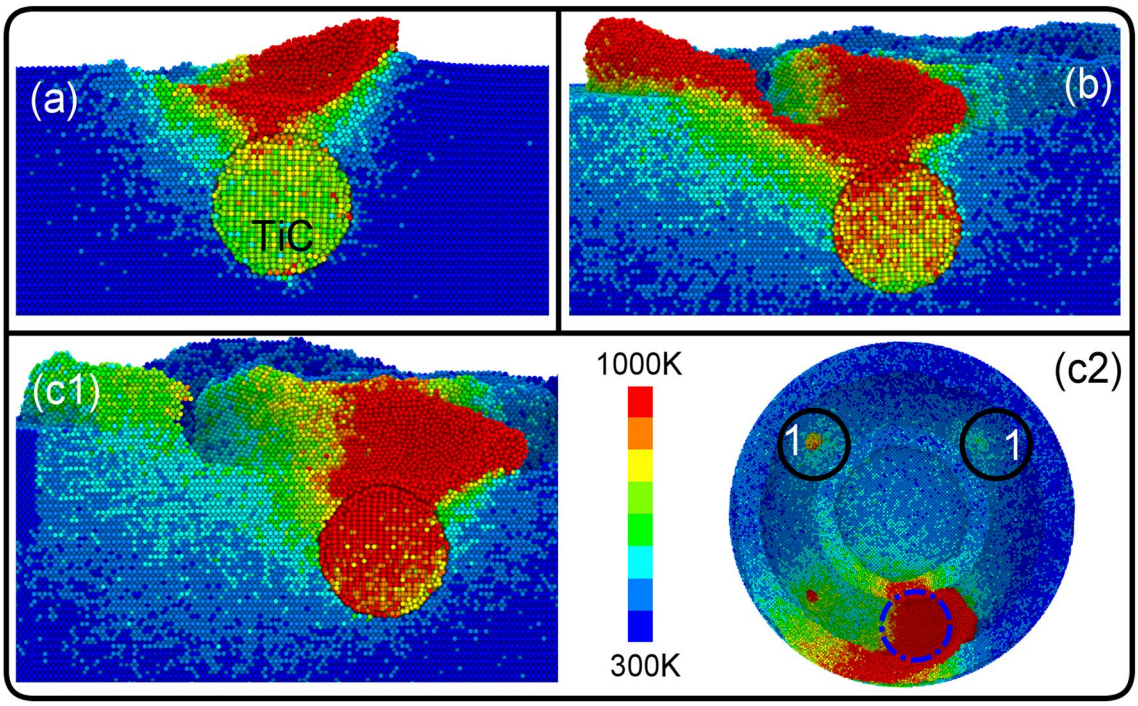

Fig. 19 Atomic friction distribution diagram of the workpiece: (**a**) first process, (**b**) second process, and (**c1**–**c2**) third process

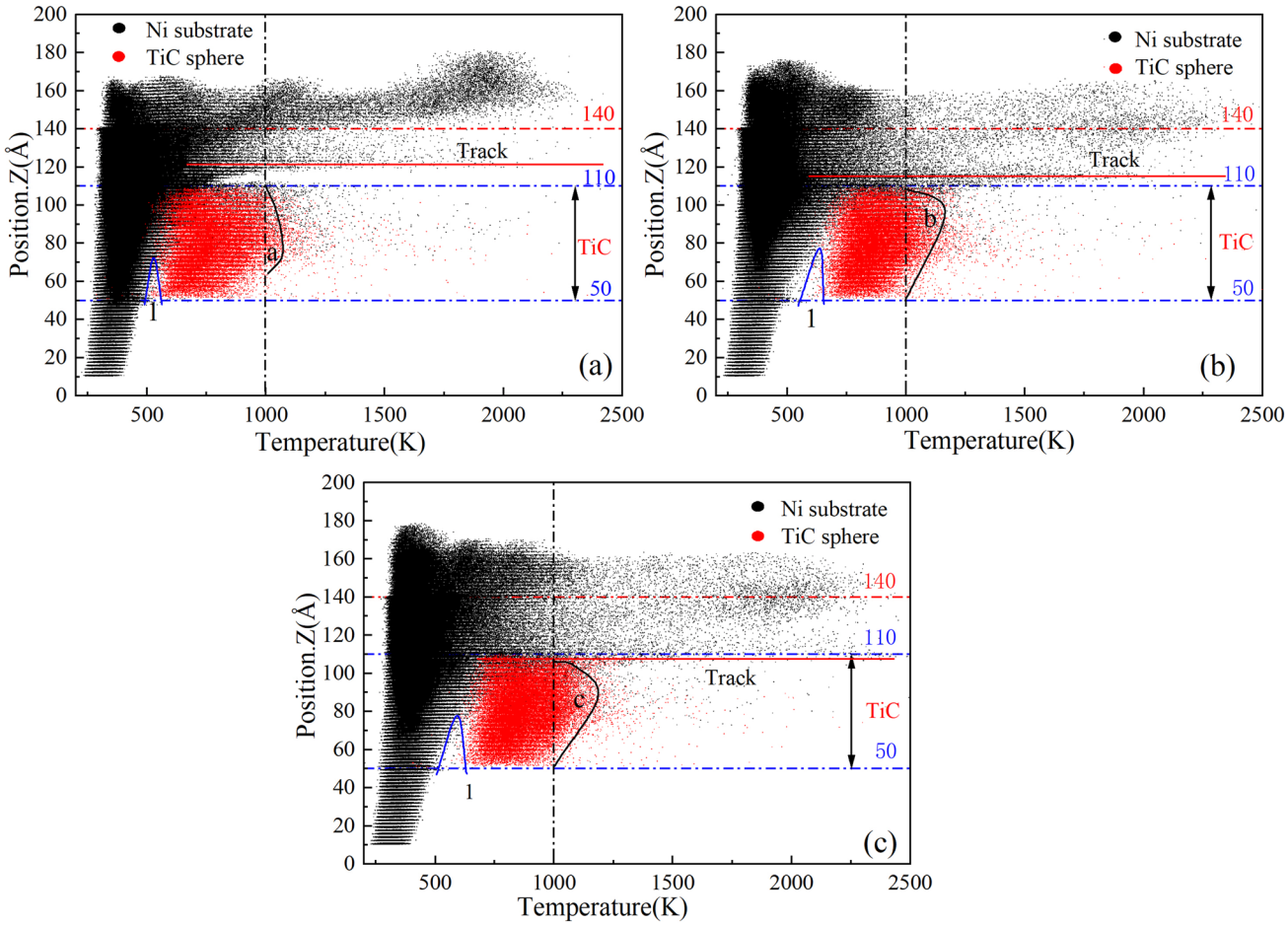

Fig. 20 Temperature scatter distribution. (**a**–**c**) Scatter plots of temperature from the first to the third friction processes

that the stability of the TiC phase structure blocks the extension and development of defects in the interior of the workpiece and a portion of the moving atoms directly act on the TiC phase. Additionally, as the number of friction atoms increases, more defects and motion of atoms act directly on the TiC phase, which increases the extrusion of the TiC phase and leads to a continuous increase in temperature. As shown in Fig. 20a–c, it is noticeable that the number of high-temperature TiC atoms above 1000 K increases continuously with the number of friction processes, As shown in Fig. 20a–c. This eventually results in increasing discontinuity in the temperature between the matrix atoms and TiC atoms. However, during the entire process, the temperature of the atoms at the lower end of the TiC phase remains essentially unchanged. These results further demonstrate that TiC has a protective effect on lower-end matrix atoms.

Figure 21 presents a graph of the friction temperature with advancing time steps, where one can see that the overall temperature of the workpiece first increases slowly and then tends to stabilize and fluctuate slightly as a result of the mutual extrusion, shearing, and friction between the grinding ball and workpiece during the friction process, which causes plastic deformation of the workpiece material

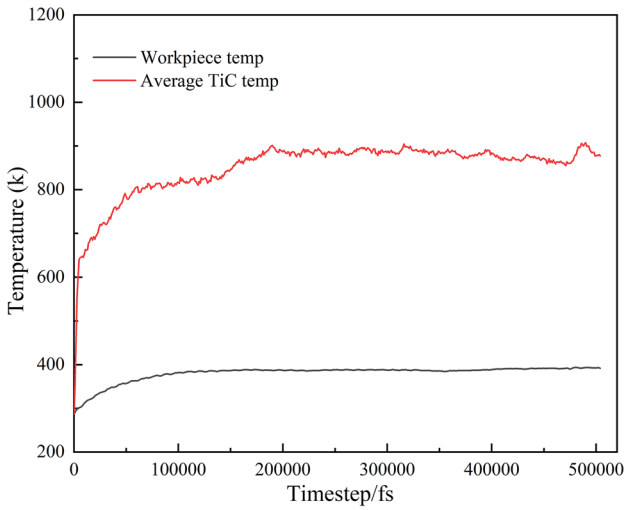

Fig. 21 Response curve of friction temperature over time

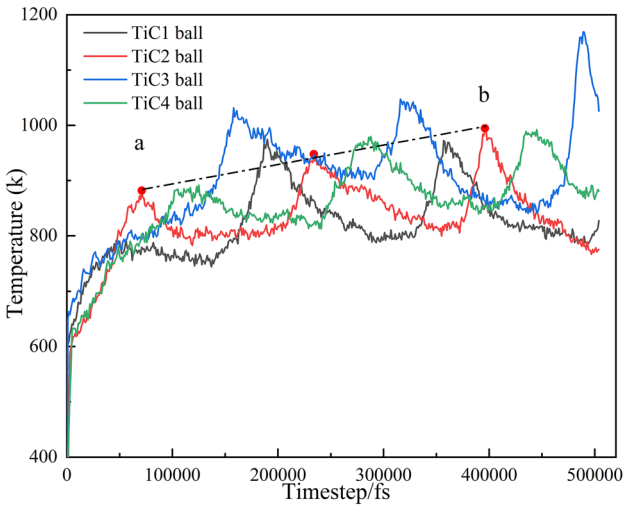

Fig. 22 Temperature response curve of the TiC ball with advancing time steps

and generates a large amount of heat energy. However, the friction initially produces fewer wear atoms that cannot carry a large amount of heat, allowing the temperature to increase slowly. As the ball is gradually pressed downward, a larger number of swarf atoms are produced, allowing the temperature to stabilize. Additionally, the increase in temperature with small fluctuations indicates dislocation nucleation and diffusion within the workpiece.

Regardless, the average temperature of the TiC atoms increases rapidly at the beginning of friction process and is higher than the average temperature of the workpiece. This is because the TiC phase is squeezed by the motion of atoms, causing the conversion of kinetic energy into heat. Simultaneously, the defects inside the workpiece act directly on the TiC phase, causing the temperature to increase rapidly above the average temperature of the workpiece. It should be noted that there are large fluctuations in the average temperature of the TiC atoms throughout the friction processes. This is a result of the non-uniformity of the dislocation nucleation and development during the entire process, which leads to discontinuities in the dislocations acting on the TiC phase, causing large fluctuations in the average temperature of the TiC atoms.

To accurately analyze the temperature variation rule of the TiC ball during the friction processes, the average temperature variation curve of the TiC ball with advancing time steps was extracted, as shown in Fig. 22. One can see that the average temperature of the TiC ball varies approximately periodically based on the extension of defects being blocked by the TiC phase each time the grinding ball reaches the vicinity of the TiC phase, which generates a large amount of heat. Additionally, the movement of some of the surrounding atoms also causes an increase in temperature. It should be noted that the peak of the average temperature of the TiC increases gradually with the number of friction processes, as shown by the straight line "ab" in Fig. 22. This is principally attributed to the fact that with an increasing number of friction processes, the distance between the grinding ball and TiC phase decreases, which gradually increases the action on the TiC phase and the number of defects that are obstructed, resulting in a gradually increasing peak in the average temperature of the TiC phase.

4 Conclusions

In this study, repeated friction processes on TiC/Ni composites were simulated using MD to systematically investigate the frictional wear mechanisms of carbides on nickel-based alloys. Our conclusions are summarized below.

During the relaxation process, with a change in system energy, the matrix nickel atoms are the first to undergo displacement deformation. The displacement is transferred to the TiC to make the entire workpiece reach equilibrium through atomic displacement adjustment. The appearance of the peak and valley values of the friction force is related to the hindrance of dislocation development inside the matrix by the TiC.

In the first friction process, the variation in the wear depth is small and the range of action of the abrasive ball on the workpiece is large. With the increase in the friction times, the maximum variation of the abrasion depth is 8.79576 Å, the range of action of the grinding ball on the workpiece decreases and the average wear rate decreases to 0.02709; when the grinding ball is located above the TiC phase under the same number of rubbings, the abrasion depth is shallow.

The displacement direction of the workpiece atoms is deflected and extends toward the interior of the workpiece when the grinding ball acts above the TiC phase. With the increase in friction times, the length of dislocations becomes longer and the number of strips increases, forming dislocation entanglement and leading to friction hardening.

During the friction process, the temperature of the workpiece atoms slowly increased to 400K, while the average temperature of TiC rapidly increased to more than 850 K. The temperature of the TiC phase reflected a certain periodicity with the relative position of the grinding balls; the temperature of TiC and matrix atoms reflected a certain discontinuity, and the temperature discontinuity gradually increased with the increase in the friction times.

Acknowledgments The project was supported by the Natural Science Foundation of Gansu Province (20JR5RA462, 20JR5RA442).

Funding Gansu Science and Technology Department (Grant Nos. 20JR5RA462, 20JR5RA442).

Declarations

Conflict of interest We declare that we have no financial and personal relationships with other people or organizations that can inappropriately influence our work, there is no professional or other personal interest of any nature or kind in any product, service and/or company that could be construed as influencing the position presented in, or the review of, the manuscript entitled, "Molecular dynamics study on the nanoscale repeated friction and wear mechanisms of TiC/Ni composites".

Ethical statement We declare that our paper has not been submitted or published elsewhere; All data in this paper are true and reliable, and the main data and charts have not been published; This article does not contain plagiarism or infringement of others' intellectual property rights; This study does not involve human or animals.

References

1. Z. Ma, Y.L. Pei, L. Luo et al., Partitioning behavior and lattice misfit of γ/γ′ phases in Ni-based superalloys with different mo additions. Rare Met. **40**, 920–927 (2021). https://doi.org/10.1007/s12598-019-01309-z
2. Y.S. Zhao, J. Zhang, F.Y. Song et al., Effect of trace boron on microstructural evolution and high temperature creep performance in re-containing single crystal superalloys. Prog. Nat. Sci. Mater. Int. **30**, 371–381 (2020). https://doi.org/10.1016/j.pnsc.2020.05.003
3. K. Patel, J. Fei, G. Liu et al., Milling investigations and yield strength calculations for nickel alloy Inconel 625 manufactured with laser powder bed fusion process. Prod. Eng. **13**, 693–702 (2019). https://doi.org/10.1007/s11740-019-00922-2
4. J. Gonzalez, J. Mireles, S. Stafford et al., Characterization of Inconel 625 fabricated using powder-bed-based additive manufacturing technologies. J. Mater. Process Technol. **264**, 200–210 (2019). https://doi.org/10.1016/j.jmatprotec.2018.08.031
5. D.D. Gu, S.N. Cao, K.J. Lin et al., Laser metal deposition additive manufacturing of tic reinforced Inconel 625 composites: influence of the additive tic particle and its starting size. J. Manuf. Sci. Eng. **139**, 200–210 (2016). https://doi.org/10.1115/1.4034934
6. D. Misra, S. Barange, H. Joardar et al., Comparative study on the tribological properties of laser post-treated and untreated AISI304 stainless steel matrix composite reinforced with hard ceramic particles (TiB2–TiN–SiC) and prepared by ex-situ P/M route. Ceram. Int. **45**, 18852–18864 (2019). https://doi.org/10.1016/j.ceramint.2019.06.119
7. J.E. Bernard, The simulation of coulomb friction in mechanical systems. Simulation **34**, 11–16 (1980)
8. G.V. Jagadeesh, S.G. Setti, A review on micromechanical methods for evaluation of mechanical behavior of particulate reinforced metal matrix composites. J. Mater. Sci. (2020). https://doi.org/10.1007/s10853-020-04715-2
9. I. Tudela, A.J. Cobley, Y. Zhang et al., Tribological performance of novel nickel-based composite coatings with lubricant particles. Friction **7**, 81–92 (2019). https://doi.org/10.1007/s40544-018-0211-0
10. S.M. Zhao, X.F. Shen, J.L. Yang et al., Densification behavior and mechanical properties of nanocrystalline tic reinforced 316L stainless steel composite parts fabricated by selective laser melting. Opt. Laser Technol. **103**, 239–250 (2018). https://doi.org/10.1016/j.optlastec.2018.01.005
11. Y.H. Lee, S. Ko, H. Park et al., Effect of TiC particle size on high temperature oxidation behavior of tic reinforced stainless steel. Appl. Surf. Sci. **480**, 951–955 (2019). https://doi.org/10.1016/j.apsusc.2019.02.138
12. L. Li, K. He, S.Y. Sun et al., High-temperature friction and wear features of nickel-based single crystal superalloy. Tribol. Lett. **68**, 26 (2020). https://doi.org/10.1007/s11249-020-1266-4
13. T. Sun, Q. Wang, D.L. Sun et al., Study on dry sliding friction and wear properties of ti2 AlN/TiAl composite. Wear **268**, 693–699 (2009). https://doi.org/10.1016/j.wear.2009.11.007
14. L. Mengis, C. Grimme, M.C. Galetz, Tribological properties of the uncoated and aluminized Ti–48Al–2Cr–2NB tial alloy at high temperatures. Wear **477**, 203818 (2021). https://doi.org/10.1016/j.wear.2021.203818
15. Y.X. Xu, M.C. Wang, F.L. Zhu et al., A molecular dynamic study of nano-grinding of a monocrystalline copper-silicon substrate. Appl. Surf. Sci. **493**, 933–947 (2019). https://doi.org/10.1016/j.apsusc.2019.07.076
16. W.S. Ko, B. Grabowski, J. Neugebauer, Development and application of a Ni–Ti interatomic potential with high predictive accuracy of the martensitic phase transition. Phys. Rev. B **92**, 134107.134101-134107.134122 (2015). https://doi.org/10.1103/PhysRevB.92.134107
17. Q. Feng, X.Y. Song, H.X. Xie et al., Deformation and plastic coordination in WC–Co composite—molecular dynamics simulation of nanoindentation. Mater. Des. **120**, 193–203 (2017). https://doi.org/10.1016/j.matdes.2017.02.010
18. S.V. Hosseini, M. Vahdati, Modeling the effect of tool edge radius on contact zone in nanomachining. Comput. Mater. Sci. **65**, 29–36 (2012). https://doi.org/10.1016/j.commatsci.2012.06.037
19. F.F. Xu, F.Z. Fang, X.D. Zhang, Effects of recovery and side flow on surface generation in nano-cutting of single crystal silicon. Comput. Mater. Sci. **143**, 133–142 (2018). https://doi.org/10.1016/j.commatsci.2017.11.002
20. F.S. Yin, X.F. Sun, J.G. Li et al., Preparation of a (ti, nb, w)c particulate reinforced nickel-base superalloy via super-high temperature treatment of melt. Mater. Lett. **57**, 3377–3380 (2003). https://doi.org/10.1016/S0167-577X(03)00078-8
21. X. Liu, Z.L. Liu, L.T. Zhang et al., Increased tensile strength and elongation of the Ni–Fe based polycrystalline cast superalloy via the trace addition of TiC nanoparticles. Mater. Sci. Eng. A **827**, 141988 (2021). https://doi.org/10.1016/j.msea.2021.141988
22. V. Testa, S. Morelli, G. Bolelli et al., Micromechanical behaviour and wear resistance of hybrid plasma-sprayed TiC reinforced tribaloy-400. Surf. Coat Technol. **425**, 127682 (2021). https://doi.org/10.1016/j.surfcoat.2021.127682
23. W.J. Lv, X.S. Yang, Y.Q. Ji et al., Effects of tic nanoparticle additions on microstructure and mechanical properties of fecral alloys prepared by directed energy deposition. J. Nucl. Mater. **554**, 15309 (2021). https://doi.org/10.1016/j.jnucmat.2021.153094
24. Y. Wang, J. Shi, Y. Wang, Reinforcing Inconel 718 superalloy by nano-tic particles in selective laser melting. City: American Society of Mechanical Engineers, Year. V002T005A018
25. Z. He, W. Wen-Xin, C. Fang et al., Microstructure manipulation and strengthening mechanisms of 40Cr steel via trace tic nanoparticles. Mater. Sci. Eng. A **822**, 141693 (2021). https://doi.org/10.1016/j.msea.2021.141693
26. M.P. Reddy, R.A. Shakoor, G. Parande et al., Enhanced performance of nano-sized sic reinforced al metal matrix nanocomposites synthesized through microwave sintering and hot extrusion techniques. Prog. Nat. Sci. Mater. Int. **27**, 606–614 (2017). https://doi.org/10.1016/j.pnsc.2017.08.015
27. B. Cai, Y.F. Tan, L. He et al., Tribological behavior and mechanisms of graphite/CaF2/TiC/Ni-base alloy composite coatings. Trans. Nonferrous Met. Soc. China **23**, 392–399 (2013). https://doi.org/10.1016/s1003-6326(13)62475-9

28. Z.H. Yin, P.Z. Zhu, B. Li, Study of nanoscale wear of SiC/Al nanocomposites using molecular dynamics simulations. Tribol. Lett. **69**, 1–17 (2021). https://doi.org/10.1007/s11249-021-01414-0
29. Z.B. Zhang, I. Alabd Alhafez, H.M. Urbassek, Scratching an Al/Si interface: molecular dynamics study of a composite material. Tribol. Lett. **66**, 1–12 (2018). https://doi.org/10.1007/s11249-018-1038-6
30. Y.Q. Wang, S. Tang, J. Guo, Molecular dynamics study on deformation behaviour of monocrystalline gan during nano abrasive machining. Appl. Surf. Sci. **510**, 145492 (2020). https://doi.org/10.1016/j.apsusc.2020.145492
31. Z.P. Hao, R.R. Cui, Y.H. Fan et al., Diffusion mechanism of tools and simulation in nanoscale cutting the Ni–Fe–Cr series of nickel-based superalloy. Int. J. Mech. Sci. **150**, 625–636 (2019). https://doi.org/10.1016/j.ijmecsci.2018.10.058
32. P. Stoyanov, L. Dawag, D.G. Goberman et al., Friction and wear characteristics of single crystal Ni-based superalloys at elevated temperatures. Tribol. Lett. **66**, 1–9 (2018). https://doi.org/10.1007/s11249-018-0994-1
33. Z.X. Zhu, B. Peng, R.C. Feng et al., Molecular dynamics simulation of chip formation mechanism in single-crystal nickel nanomachining. Sci. China-Technol. Sci. **62**, 1916–1929 (2019). https://doi.org/10.1007/s11431-019-9520-8
34. Y.M. Kim, B.J. Lee, Modified embedded-atom method interatomic potentials for the Ti–C and Ti–N binary systems. Acta Mater. **56**, 3481–3489 (2008). https://doi.org/10.1016/j.actamat.2008.03.027
35. M.G. Elkhateeb, Y.C. Shin, Molecular dynamics-based cohesive zone representation of ti6al4v/tic composite interface. Mater. Des. **155**, 161–169 (2018). https://doi.org/10.1016/j.matdes.2018.05.054
36. S.M. Foiles, M.I. Baskes, M.S. Daw, Embedded-atom-method functions for the fcc metals Cu, Ag, Au, Ni, Pd, Pt, and their alloys. Phys. Rev. B **33**, 7983–7991 (1986). https://doi.org/10.1103/physrevb.33.7983
37. Q.H. Fang, Q. Wang, J. Li et al., Mechanisms of subsurface damage and material removal during high speed grinding processes in Ni/Cu multilayers using a molecular dynamics study. RSC Adv. **7**, 42047–42055 (2017). https://doi.org/10.1039/c7ra06975h
38. Tersoff, Modeling solid-state chemistry: interatomic potentials for multicomponent systems. Phys. Rev. B **39**, 5566–5568 (1989)
39. Q. Zhang, D.F. Diao, M. Kubo, Nanoscratching of multi-layer graphene by molecular dynamics simulations. Tribol. Int. **88**, 85–88 (2015). https://doi.org/10.1016/j.triboint.2015.03.004
40. J.F. Archard, Contact and rubbing of flat surfaces. J. Appl. Phys. **24**, 981–988 (1953). https://doi.org/10.1063/1.1721448
41. F.F. Xu, F.Z. Fang, X.D. Zhang, Hard particle effect on surface generation in nano-cutting. Appl. Surf. Sci. **425**, 1020–1027 (2017). https://doi.org/10.1016/j.apsusc.2017.07.089
42. A. Stukowski, V.V. Bulatov, A. Arsenlis, Automated identification and indexing of dislocations in crystal interfaces. Model Simul. Mater. Sci. **20**, 085007–085023 (2012). https://doi.org/10.1088/0965-0393/20/8/085007
43. D.A. Porter, K.E. Easteling, *Phase Transformations in Metals and Alloys* (Chapman Hall, London, 1981)
44. Y.F. Yang, H.Y. Wang, J. Zhang et al., Lattice parameter and stoichiometry of ticxproduced in the Ti–C and Ni–Ti–C systems by self-propagating high-temperature synthesis. J. Am. Ceram. Soc. **91**, 2736–2739 (2008). https://doi.org/10.1111/j.1551-2916.2008.02486.x
45. Z.X. Zhu, Y. Gong, Y.D. Zhou et al., Molecular dynamics simulation of single crystal nickel nanometric machining. Sci. China Technol. Sci. **59**, 867–875 (2016). https://doi.org/10.1007/s11431-016-6061-y
46. Z.B. Zhang, H.M. Urbassek, Dislocation-based strengthening mechanisms in metal–matrix nanocomposites: a molecular dynamics study of the influence of reinforcement shape in the Al–Si system. Comput. Mater. Sci. **145**, 109–115 (2018). https://doi.org/10.1016/j.commatsci.2017.12.063
47. S. Chen, Z.H. Aitken, Z.X. Wu et al., Hall-petch and inverse hall-petch relations in high-entropy conifealxcu1-x alloys. Mater. Sci. Eng. A **773**, 138873.138871-138873.138879 (2020). https://doi.org/10.1016/j.msea.2019.138873
48. R.P. Patil, D. Doan, Z.H. Aitken et al., Hardening in Au–Ag nanoboxes from stacking fault-dislocation interactions. Nat. Commun. **11**, 1–9 (2020). https://doi.org/10.1038/s41467-020-16760-1